White Rose
university consortium
Universities of Leeds, Sheffield & York

eprints@whiterose.ac.uk
https://eprints.whiterose.ac.uk/

THz waveguide adapters for efficient radiation out-coupling from double metal THz QCLs

Fabrizio Castellano,[1,*] Lianhe Li,[2] Edmund H. Linfield,[2] A. Giles Davies,[2] Harvey E. Beere,[3] David A. Ritchie,[3] and Miriam S. Vitiello[1]

[1]NEST, CNR - Istituto Nanoscienze and Scuola Normale Superiore, Piazza San Silvestro 12, 56127, Pisa, Italy
[2]School of Electronic and Electrical Engineering, University of Leeds, Leeds LS2 9JT, UK
[3]Cavendish Laboratory, University of Cambridge, Cambridge CB3 0HE, UK
[*]fabrizio.castellano@nano.cnr.it

Abstract: We report the development of on-chip optical components designed to improve the out-coupling of double-metal terahertz (THz) frequency quantum cascade lasers (QCLs). A visible reshaping of the optical beam is achieved, independent of the precise waveguide configuration, by direct incorporation of cyclic-olefin copolymer (COC) dielectric optical fibers onto the QCL facet. A major improvement is further achieved by incorporating a micromachined feed-horn waveguide, assembled around the THz QCL and integrated with a slit-coupler. In its first implementation, we obtain a $\pm 20°$ beam divergence, offering the potential for high-efficiency radiation coupling from a metal-metal waveguide into optical fibers.

1. Introduction

Whilst the visible, infrared and microwave ranges of the electromagnetic spectrum benefit from established signal routing and processing components, the terahertz (THz) frequency range still requires a suitable framework of equivalent components. The particular length scale that characterizes THz radiation makes it unclear whether passive components and circuitry in this range should be developed mimicking optics or electronics. Limitations come partly from the lack of highly transparent materials, and partly from the difficulty of focusing and routing radiation from and to components that are smaller than the wavelength. In terms of sources, despite their need for cryogenic cooling, THz quantum cascade lasers (QCL) [1, 2] are the only high spectral purity [3] solid state sources that can provide hundreds of mW levels of power in the 2-5 THz band [4, 5]. One of the key issues in THz QCL technology is, however, the divergence of the outcoming beams: in a standard edge emitting configuration the radiation is emitted in a beam with approximately 30° divergence for single-plasmon waveguides [6], whereas an almost isotropic emission, rich in fringes, is seen for the case of double-metal [7] waveguides.

This is principally due to diffraction at the subwavelength-sized laser facet, and interference between emissions from the two cleaved facets. Low divergence double-metal devices have been realized over the last few years, principally by exploiting lithographic approaches based on engineering third-order distributed feedback gratings [8], plasmonic collimators [9], circular resonator approaches for vertical emission [10], photonic crystals [11] and quasi-crystals [12].

Although very effective, these approaches operate at a fixed frequency, whilst manipulation of multimode or broadly tunable single mode sources is often necessary to address specific spectroscopic or metrological applications. As alternative broadband solutions to improve the beam quality and reduce the impedance mismatch between the waveguide and free space, hyperhemispherical silicon lenses [13], three-dimensional [14–16] or planar horn antennas [17] and patch antenna arrays [18] have been proposed. The approaches reported in [14–16] provide reduced divergence of the output beam through assembly of an external component aligned to the laser facet, while the monolithic solutions in [17, 18] provide a more divergent beam but with the advantage of a planar process. As an alternative possibility one can consider high coupling efficiency THz waveguides as mode cleaners.

THz waveguides have already been demonstrated in a number of implementations including parallel plate waveguides [19], thin metallic wires [20] and dielectric optical fibers [21].

Recently, hollow core waveguides, with a sequence of different metallic or dielectric inner coatings, with transmission losses as low as 1.5 dB/m [22–24], have been coupled with linearly and azimuthally polarized THz QCLs or stitched on the QCL facet [25]. Alternatively, direct coupling of a single-plasmon THz QCL to a polymeric optical fiber made of cyclic-olefin copolymer (COC) has been reported [26], enabling narrowing of the output beam shape.

Despite the clear advantages, in all the mentioned approaches the large impedance mismatch between the QCL and the waveguide itself, limits the range of applications of this combined coupled system, even more when a double metal QCL waveguide is considered. An efficient, impedance matched coupling of a THz source with an external waveguide would open up new possibilities for present THz systems.

In this work, we address this issue by designing and developing a novel approach to couple THz radiation from a double-metal QCL into an on-chip hollow rectangular waveguide feeding a triangular horn, with the specific aim of optimizing the optical beam divergence. By comparing this approach with a simpler external waveguide coupling, we show improved out-coupling with respect to a COC fiber- coupled double-metal THz QCL.

2. Direct coupling of a double-metal THz QCL to a polymeric optical fiber

As a first step, following the same approach of our previous work [26] we glued a section of a COC optical fiber to the facet of a double-metal THz QCL. COC was selected because of its high transparency in the THz range [27] (with absorption of only ~1 cm^{-1} at 3 THz and a refractive index of 1.52) and its low temperature thermoplastic character that makes its processing compatible with THz QCLs. The optical fiber was fabricated by hand-drawing from a crucible of molten COC, obtaining about 1 m of fiber with a diameter between 100 µm and 500 µm. A 7 mm long fiber section, with a 300 µm diameter, was then cut with a razor blade and attached to the laser facet (see schematic in Fig. 1(a)). The assembly of the optical fiber on the laser was performed by heating the laser to 130°C and then letting one end of the fiber melt onto the laser facet. The QCL employed had a 10 µm thick active-region, based on the three-well design (wafer V569) reported in [28] and was processed into a 100 µm wide double-metal waveguide. The measured emission spectra showed multi-mode emission at a central frequency of 3.1 THz.
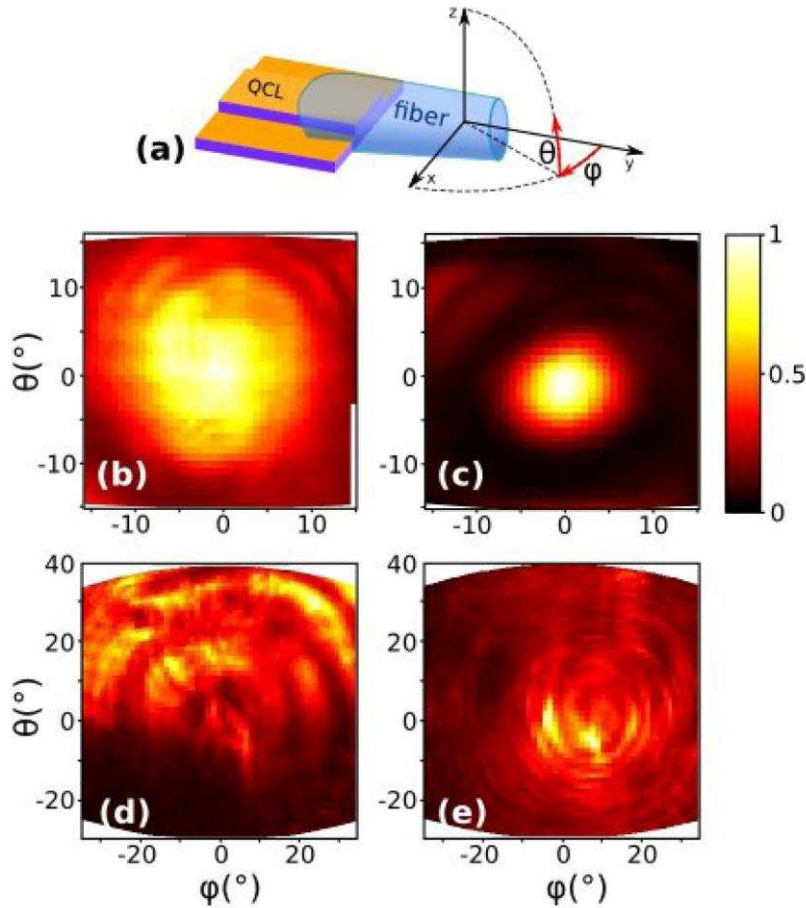

Fig. 1.   (a) Schematic diagram showing a dielectric fiber attached to the facet of a double-metal QCL; the spherical reference frame of the far-field apparatus is also indicated.
(b,c) Far-field emission pattern of a single-plasmon THz QCL without and with a coupled fiber, respectively
(d,e) Far-field emission pattern of the double-metal THz QCL without and with a coupled fiber, respectively. The color scale represents normalized angular power density.

Figure 1(a) shows the orientation of a sample with respect to the spherical reference frame, and a schematic of a laser coupled with the optical fiber section. Figure 1 shows the comparison between the far-field patterns obtained for the single-plasmon THz QCLs (see Figs. 1(b)-1(c)), and a double-metal QCL (see Figs. 1(d)-1(e)) having identical dimensions (100µm x 1mm) with and without coupling to the fiber. Intensity measurements in the far-field were performed by scanning a 3 mm diameter pyroelectric detector on a plane parallel to the laser facet, at about 7 cm distance.

The data were then mapped into spherical coordinates and corrected to account for the varying distance and orientation of the detector with respect to the laser facet. In the single-plasmon QCL we observed a 50% reduction in the beam divergence owing to the radiation being coupled into one end of the fiber, guided by total internal reflection and then emitted from the opposite end, without stray radiation exiting the fiber. When a double-metal waveguide is employed, the situation is complicated by the fact that the QCL has a very broad far-field emission (see Fig. 1(d)) and is normally multimode. The critical angle for total internal reflection in the fiber is 41°, thus not all the light emitted from the double-metal waveguide can be guided through it. This leads to stray emissions at large angles, with clear interference in the far-field due to radiation emitted from the rear facet and the presence of multiple optical modes. Despite a clear beam narrowing being visible from the comparison between Figs. 1(d) and

1(e), the beam profile achieved is still far from the single-lobe shape seen for single-plasmon QCLs. The direct coupling technique here is therefore less effective owing to the inherent fundamental limitations posed by the double-metal resonator geometry.

3. Design and fabrication of waveguide couplers

To overcome the limitations of the direct coupling of THz radiation into a fiber, we introduced additional waveguide components that were assembled on-chip on the top of double-metal THz QCLs, with the double purpose of reducing the facet reflectivity and improving the power extraction over a large frequency band.

Our extractor is composed of three parts: a series of slits patterned at the end of the laser top contact (slit coupler), a metallic waveguide section (feeder) assembled on top of the laser itself, and an adiabatic expansion of the feeder, forming a horn that radiates into an optical fiber or, alternatively, into free space. This external component containing the feeder and horn will be called a waveguide coupler in the following. Although the final goal of this device is to couple radiation into a COC optical fiber, we here report on a waveguide coupler designed to radiate into the free space, leaving the fiber coupling as a future development. Figure 2(a) shows a schematic of the device, drawn as a section of the assembly along a plane passing through the middle of the laser ridge. A standard double-metal process was employed for the fabrication of the QCL ridges. The active region (wafer L1023) was based on the three-well resonant photon design that was successfully exploited to achieve lasing up to 200 K [29], with the 10 μm thick active region processed into 100 μm wide laser ridges using wet etching. The devices have one cleaved facet and one etched facet. The top Cr/Au (10/200 nm) contact was patterned towards the side closest to the etched facet by opening four rectangular slits.

To design the waveguide coupler we employed a commercial software package (COMSOL multiphysics) to perform finite element simulations of the electromagnetic field distribution. It is important that the feeder section has the correct thickness, so that the surface plasmons on the metallic wall of the feeder can couple with the electric field leaking out of the slit coupler and the laser facet.

The feeder was designed with a 10 μm height. The slits have a pitch of 42 μm and their respective widths, starting from the slit closest to the etched facet of the QCL are 14/10/12/9 μm. These apertures, together with the laser facet itself, are designed to work as a directional coupler when the QCL waveguide is put in close proximity with a metallic plane on top of the ridge, which is provided by the feeder [26]. The slit widths were optimized through 2D finite elements simulations of the QCL coupled to the feeder. Figure 2(b) shows the frequency dependence of the simulated facet reflectivity and coupling coefficients. The forward coupling coefficient is defined as the fraction of power coupled in the direction of the horn, while the backward coupling coefficient indicates the fraction of power coupled in the opposite direction. It can be seen that the facet reflectivity lies below −3dB in the 2.8-3.25 THz band.

Also, the forward coupling is always greater than the backward coupling in the same band. The power reflection coefficient of the horn aperture radiating into free space is 0.25 according to our simulations. The waveguide coupler was micromachined into bulk GaAs by wet etching using an $H_2SO_4{:}H_2O_2{:}H_2O$ (3:3:10) solution. Scanning electron microscope (SEM) images of the couplers are shown in Figs. 2(c)-2(e).

Each feeder is 200 μm wide and 20 μm deep, and is followed by a staircase that forms the horn, that in turn leads to the output aperture. The staircase shape was obtained by ten iterations of UV optical lithography and etching. Depending on the relative orientation of the lithographic mask with respect to the GaAs crystal, different etching behaviors were obtained. Figure 2(c) shows an array of waveguide couplers oriented along the ⟨011⟩ direction, while Fig. 2(d) reproduces orientations along the ⟨01$\bar{1}$⟩ direction.

In the two cases, the wet etching undercut behaves differently. For Fig. 2(c) a flat-bottom horn is obtained for every etching step and a large lateral undercut is formed, therefore posing a limit on the maximum achievable depth of the horn due to mechanical instability of the photoresist in the undercut region. Conversely, in Fig. 2(d), there is negligible undercut, and the horn depth is now limited by the precise position at which the trench sidewalls meet each other at the apex of a triangle. We have fabricated couplers exploiting both geometrical configurations. In both cases, the horns are produced in large arrays (see Fig. 2(c)) with the same pitch as the QCL ridges (500μm), metallized with an evaporated Cr/Au 10/200 nm coating, and then cleaved in chips containing two couplers each (see Fig. 2(d)). Finally, the double horn chip is flipped upside down and mounted onto the QCL by hand. Figure 2(e) shows the final device configuration, in which two laser ridges are inserted into the waveguide section of the couplers.

To combine together the coupler and the QCL we glued them by leaking optical photoresist into one of the two waveguide couplers (right-side coupler in Fig. 2(e)). This was achieved after the QCL chip had been indium-soldered on a copper mount, wire bonded and tested. Capillary forces, operating before the photoresist is baked, center the waveguide couplers on the laser ridges along the x direction (perpendicular to the laser ridge).

Along the y direction (parallel to the laser ridge) the alignment of the waveguide adapter and the QCL is manual, and can result in two different configurations, schematically shown in Figs. 2(f) and 2(g). In the first case (see Fig. 2(f)), the slit-coupler patterned at the edge of the QCL is inserted inside the horn of the waveguide coupler, providing a lower coupling to the feeder, while in the second geometry (see Fig. 2(g)) it is located inside the waveguide section, allowing the feeder to be coupled with the QCL, as designed.
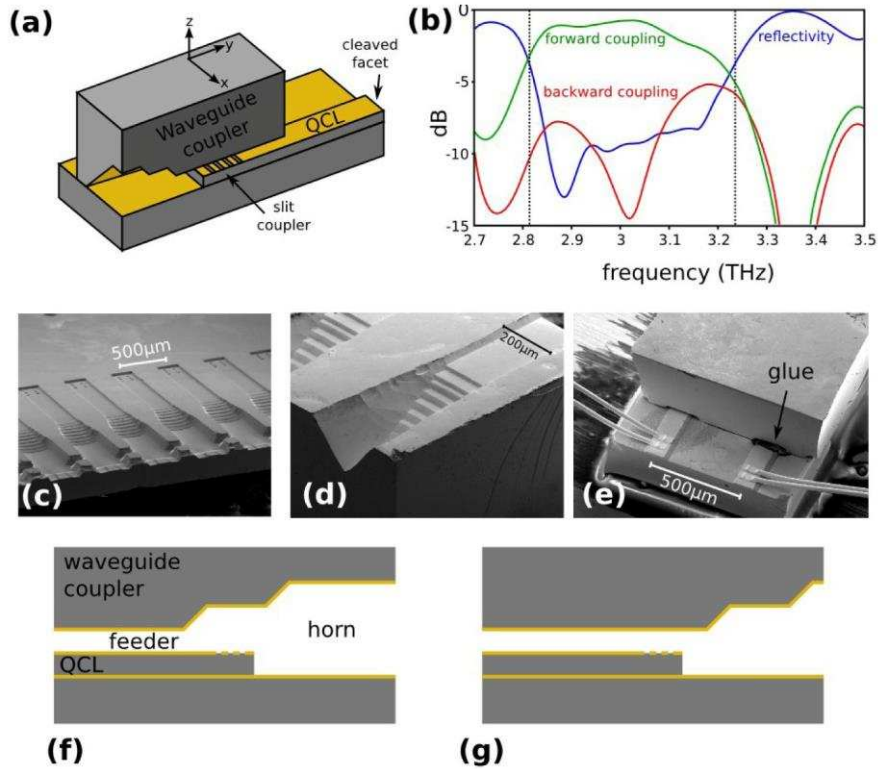
Fig. 2. (a) Device schematics: yellow areas indicate metallized surfaces, gray areas correspond to GaAs.
(b) Simulated reflectivity, forward and backward coupling coefficients of the waveguide coupler as a function of the frequency.
(c) Scanning electron microscope (SEM) image of an array of waveguide couplers aligned along the ⟨011⟩ direction prior to cleaving.
(d) SEM image of the cleaved chip containing two waveguide couplers aligned along the ⟨01$\bar{1}$⟩ direction
(e) SEM image of the final assembly, taken from the cleaved facet side.
(f,g) Schematics of two alternative alignment configurations of the slit-coupler with respect to the feeder and the horn, respectively.

4. Results

Three different device architectures were developed and tested. Sample A is a double metal QCL with patterned slit-coupler; sample B is a double metal QCL embedded (with patterned split-coupler) below the waveguide coupler shown in Fig. 2(c) and assembled in the configuration schematically sketched in Fig. 2(f). Sample C exploits the waveguide coupler of Fig. 2(d) and assembly configuration of Fig. 2(g). All results refer to the photoresist-free device (the left device in Fig. 2(e)), as optical absorption in the waveguide coupler led to worse overall performance for the devices filled with photoresist. For each sample, we measured the light-current-voltage (LIV) characteristics and far-field patterns. Emission spectra of samples A and C were collected in rapid-scan mode employing a Fourier transform infrared spectroscopy system. It is worth mentioning that the assembly of the waveguide coupler on the QCL is achieved by gluing it with photoresist, meaning that it is a reversible process which allows one to disassemble the coupler without damaging the QCL ridge simply by removing the photoresist with acetone. The three samples reported here share the same THz QCL device, sequentially assembled with two different waveguide couplers. We also tested the QCL without the waveguide coupler before and after the set of measurements presented here, finding no difference in the LIV curves, therefore confirming that the coupler assembly and disassembly process does not introduce any damage to the THz QCL, and preserves its electrical and optical performance.

4.1 Far-field patterns

The far-field pattern of each sample was measured in the same experimental setup described in section 2. The detector distance from the sample was set to 4 cm in order to maximize the experimental angular range. All measurements were performed in a closed-cycle refrigerator with samples biased with 200 ns pulses at a 50 kHz repetition rate. Figures 3(a)-3(c) show the measured far-field patterns of samples A, B and C, respectively. The color scale represents normalized angular power density. Figures 3(d)-3(f) show the simulated electric field profile of the coupled waveguide mode that radiates into free space. In the case of sample A, the electric field profile corresponds to the fundamental QCL waveguide mode, whilst in the case of samples B and C the horn mode is dominating. The two different mounting configurations of samples B and C (Figs. 2(f) and 2(g), respectively) do not affect which horn mode is excited. Sample A exhibits the typical double metal far-field pattern, with an emission spanning a broad angular range, especially in the vertical direction. In this case, the signal at negative angles is almost absent because emission takes place from an etched, rather than a cleaved facet.
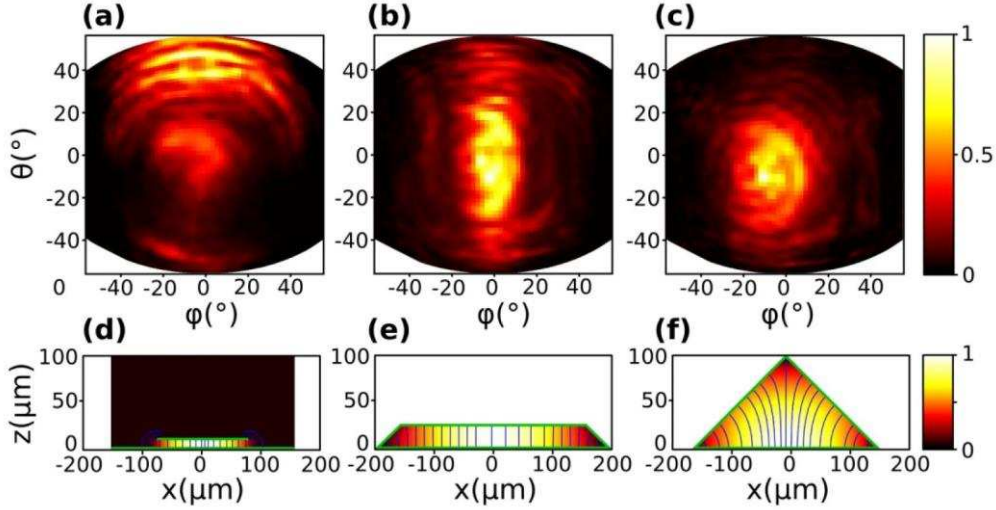
Fig. 3. (a-c) Far field emission patterns of samples A (a), B (b) and C (c). The angular reference frame and color scale correspond to those in Figs. 1(d)-1(f) electric field profiles of the waveguide modes that radiate into free space for samples A, B and C respectively. The green borders represent perfect electric conductors, the blue lines are the electric field lines, and the color scale represents the amplitude of the electric field.

Sample B had a waveguide coupler terminating with a 250 μm x 25 μm horn (see Fig. 3(e)). Its far field pattern extends approximately 30° in the horizontal direction and 60° in the vertical direction, with numerous interference fringes in the vertical direction. The broad (narrow) angular emission corresponds to the narrower (broader) waveguide dimensions. In the case of sample C, the far field emission is more symmetric and has a full divergence at half maximum of about 40° without fringes at high angles. This results from the field distribution in the triangular horn aperture, pictured in Fig. 3(f), which goes to zero at the apex of the triangle due to the boundary conditions imposed by the metallic walls on the tangential field components. For completeness, it should be mentioned that the modes pictured in Fig. 3(e)-3(f) are not the only ones that can be excited over the frequency of operation of the QCL (see section 4.3). However, the polarization of the electric field imposed by the intersubband transitions in the QCL (z direction) excludes excitation of modes with an electric field polarized along the x direction, and the position of the laser ridge in the center of the horn favors excitation of modes with a maximum at $x = 0$. Thus, while we cannot exclude the presence of excited higher order modes in the horn, we can safely conclude that the modes depicted in Figs. 3(e)-3(f) are the dominant ones. This is also confirmed by the fact that the far field patterns are single lobed and with a maximum at the origin.

4.2   LIV characteristics

Figure 4 shows the LIV characteristics of samples A, B and C, respectively. The measurement was performed in a closed cycle refrigerator at a temperature of 10 K, collecting the light using a pyroelectric detector (3 mm diameter) at about 5 cm distance from the laser facet. The device was driven in pulsed mode with 200 ns pulses at a 25 kHz repetition rate.

In order to maximize the collection efficiency, the absolute power levels shown in the plots were obtained by integrating the far-field patterns. While this leads to a collection efficiency of almost 100% for samples B and C, for sample A this value is lower because the far field extends beyond the collection range of our apparatus. We believe, though, that the power levels of samples A and B are approximately the same. Sample C on the other hand exhibits a maximum power level that is approximately half that of sample B, with a slope efficiency of about 20mW/A. All samples operate up to a heat sink temperature of ~130 K. The threshold current measured for samples A and B are consistent with that observed for cleaved devices, meaning that the presence of the slits on the top contact does not affect mirror losses significantly when the QCL waveguide is not coupled with the feeder of the waveguide coupler. On the other hand, sample C has different threshold dynamics. Whilst laser emission starts at the same current value in samples A and B, the emitted power immediately drops as the current increases and then rises again. We ascribe this behavior to the increased mirror losses within the waveguide coupler bandwidth due to the interaction of the slit extractor with the feeder, as explained in the next section.
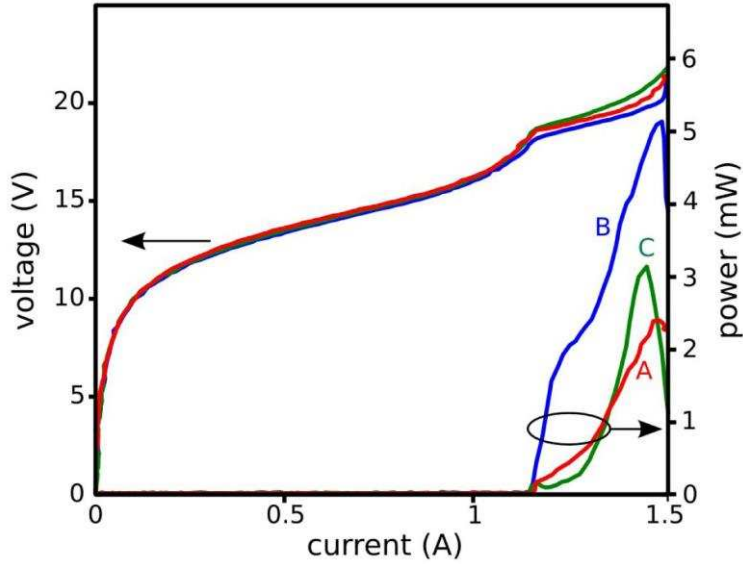
Fig. 4. Light current voltage (LIV) characteristics of samples A, B and C. The devices have been driven in pulsed mode with 200 ns wide pulses at 25 kHz repetition rate, and cooled to 10K in a closed cycle refrigerator.

4.3   Emission spectra

We measured the emission spectra of samples A and C using a Fourier-transform infrared spectrometer equipped with a silicon bolometer cooled at 4 K. The samples were cooled to 20 K in a liquid helium flow cryostat and driven in pulsed mode, with 200 ns pulses at a repetition rate of 5 kHz.

Figures 5(a)-5(b) show the normalized spectra of samples A and C, respectively, measured at different current levels. Sample A has a multimode emission from 3.05 THz to 3.48 THz across the whole bias range. The different modes, equally spaced, correspond to longitudinal Fabry-Perot modes associated with the same transverse mode. This wide-ranging emission reflects the broad gain spectrum of the active region. Sample C, on the other hand, shows a less rich spectrum. At threshold, the device emits almost single mode, with most of the power concentrated at 3.34 THz, a mode that is absent in the emission of sample A but whose position is consistent with the multiple spacing of its Fabry-Perot modes. This mode remains dominant across most of the bias range. On the contrary, the spectrum of sample A is more unstable, with optical power redistributing across different modes as the bias changes. The radically different beam shape of the two devices (see Figs. 3(a) and 3(c)) results in a different collection efficiency of each mode in the FTIR. For the case of sample C, all modes are equally collected by the f/1 optics at the entrance of the spectrometer, while this is not the case for sample A, where different modes experience different collection efficiency. However, this effect alone is not sufficient to explain the major differences in the two sets of spectra. The difference is mostly an effect of the reduced facet reflectivity due to the presence of the waveguide coupler. As shown in Fig. 2(b), in the case of sample C, the reflectivity of the QCL facet is indeed reduced to less than 0.5 in the 2.8-3.25 THz band, compared to the value of 0.95 typical of standard double metal waveguide. This means that modes in this range experience a lower modal gain due to increased mirror losses. However, since the gain bandwidth of the active region extends beyond the low-reflectivity band of our coupler [29], lasing above 3.25 THz can still occur with the same threshold current of sample A. The mode at 3.34 THz (see Fig. 5(b)) is located at a resonant frequency of the waveguide coupler where the facet reflectivity is maximum, as predicted by the simulations in Fig. 2(b). Since the spectral gain shifts with voltage, and both the facet reflectivity and forward coupling coefficient are not spectrally flat, the modal gain and out-coupling efficiency experienced by the different Fabry-Perot modes have a complex dependency on the bias, as reflected in the LI curve of sample C. We conclude that our waveguide coupler, besides improving the beam divergence of the double metal QCL, also changes the facet reflectivity enough to induce visible changes in the QCL emission spectrum and LI curve.
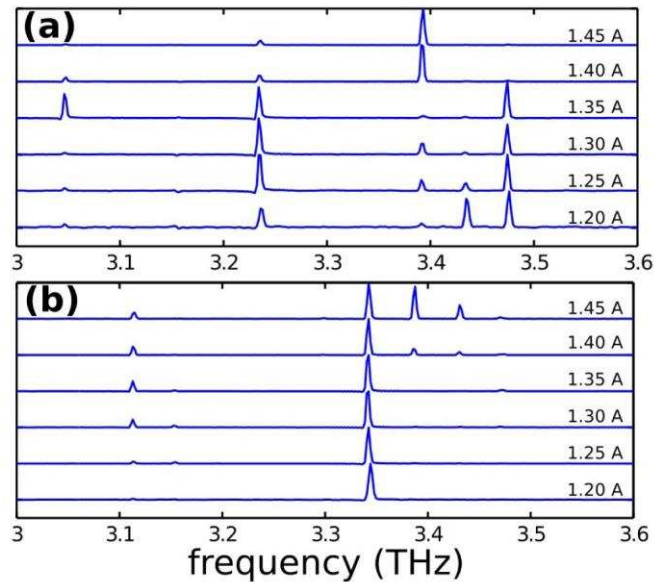
Fig. 5. Normalized emission spectra of sample (a) A and (b) C measured with a Fourier-transform infrared spectrometer for various current levels, indicated on the right for each plot.

5 Conclusions and perspectives

In conclusion, we have developed a waveguide component that is capable of efficiently shaping the output beam profile from a double metal THz QCL. Based on the threshold behavior and emission spectra, we also conclude that the waveguide adapter is able to affect the mirror losses significantly over its designed operation bandwidth. Further optimization is possible, based on the flexibility offered by the many geometrical parameters present in the design of the waveguide out-coupler. Indeed, the possibility to reduce the facet reflectivity and at the same time to improve the output beam shape, with an external component that can be assembled on top of an existing QCL, opens the way to the realization of more complex systems such as QCL amplifiers and external cavity tuners. Moreover, this component could be employed to couple radiation efficiently into a COC optical fiber, opening up the possibility of developing pig-tailed THz QCL technology suitable for multi-spectroscopy applications, injection seeding and metrological approaches across the far-infrared spectral range.

References

1. S. Kumar, "Recent progress in terahertz quantum cascade lasers," IEEE J. Sel. Top. Quantum Electron. **17**(1), 38–47 (2011).
2. M. S. Vitiello and A. Tredicucci, "Tunable emission in THz quantum cascade lasers," IEEE Trans. Thz Sci. Technol. **1**(1), 76–84 (2011).
3. M. S. Vitiello, L. Consolino, S. Bartalini, A. Taschin, A. Tredicucci, M. Inguscio, and P. De Natale, "Quantum-limited frequency fluctuations in a terahertz laser," Nat. Photonics **6**(8), 525–528 (2012).
4. A. Valavanis, J. Zhu, J. Freeman, L. Li, L. Chen, A. G. Davies, E. H. Linfield, and P. Dean, "Terahertz quantum cascade lasers with >1 W output powers," Electron. Lett. **50**(4), 309–311 (2014).
5. M. Brandstetter, C. Deutsch, M. Krall, H. Detz, D. C. MacFarland, T. Zederbauer, A. M. Andrews, W. Schrenk, G. Strasser, and K. Unterrainer, "High power terahertz quantum cascade lasers with symmetric wafer bonded active regions," Appl. Phys. Lett. **103**(17), 171113 (2013).
6. R. Köhler, A. Tredicucci, F. Beltram, H. E. Beere, E. H. Linfield, A. G. Davies, D. A. Ritchie, R. C. Iotti, and F. Rossi, "Terahertz semiconductor-heterostructure laser," Nature **417**(6885), 156–159 (2002).
7. M. Brandstetter, M. Krall, C. Deutsch, H. Detz, A. M. Andrews, W. Schrenk, G. Strasser, and K. Unterrainer, "Influence of the facet type on the performance of terahertz quantum cascade lasers with double-metal waveguides," Appl. Phys. Lett. **102**(23), 231121 (2013).

8. M. I. Amanti, G. Scalari, F. Castellano, M. Beck, and J. Faist, "Low divergence Terahertz photonic-wire laser," Opt. Express **18**(6), 6390–6395 (2010).

9. N. Yu, Q. J. Wang, M. A. Kats, J. A. Fan, S. P. Khanna, L. Li, A. G. Davies, E. H. Linfield, and F. Capasso, "Designer spoof surface plasmon structures collimate terahertz laser beams," Nat. Mater. **9**(9), 730–735 (2010).

10. L. Mahler, A. Tredicucci, F. Beltram, C. Walther, J. Faist, B. Witzigmann, H. E. Beere, and D. A. Ritchie, "Vertically emitting microdisk lasers," Nat. Photonics **3**(1), 46–49 (2009).

11. Y. Chassagneux, R. Colombelli, W. Maineult, S. Barbieri, H. E. Beere, D. A. Ritchie, S. P. Khanna, E. H. Linfield, and A. G. Davies, "Electrically pumped photonic-crystal terahertz lasers controlled by boundary conditions," Nature **457**(7226), 174–178 (2009).

12. M. S. Vitiello, M. Nobile, A. Ronzani, A. Tredicucci, F. Castellano, V. Talora, L. H. Li, E. H. Linfield, and A. G. Davies, "Photonic quasi-crystal terahertz lasers," Nat. Commun. **5**, 5884 (2014).

13. A. Wei Min Lee, Q. Qin, S. Kumar, B. S. Williams, Q. Hu, and J. L. Reno, "High-power and high-temperature THz quantum-cascade lasers based on lens-coupled metal-metal waveguides," Opt. Lett. **32**(19), 2840–2842 (2007).

14. M. I. Amanti, M. Fischer, C. Walther, G. Scalari, and J. Faist, "Horn antennas for terahertz quantum cascade lasers," Electron. Lett. **43**(10), 573–574 (2007).

15. W. Maineult, P. Gellie, A. Andronico, P. Filloux, G. Leo, C. Sirtori, S. Barbieri, E. Peytavit, T. Akalin, J.-F. Lampin, H. E. Beere, and D. A. Ritchie, "Metal-metal terahertz quantum cascade laser with micro-transverse-electromagnetic-horn antenna," Appl. Phys. Lett. **93**(18), 183508 (2008).

16. J. Lloyd-Hughes, G. Scalari, A. van Kolck, M. Fischer, M. Beck, and J. Faist, "Coupling terahertz radiation between sub-wavelength metal-metal waveguides and free space using monolithically integrated horn antennae," Opt. Express **17**(20), 18387–18393 (2009).

17. A. Brewer, J. R. Freeman, P. Cavalié, J. Maysonnave, J. Tignon, S. S. Dhillon, H. E. Beere, and D. A. Ritchie, "Coherent detection of metal-metal terahertz quantum cascade lasers with improved emission characteristics," Appl. Phys. Lett. **104**(8), 081107 (2014).

18. C. Bonzon, I. C. Benea Chelmus, K. Ohtani, M. Geiser, M. Beck, and J. Faist, "Integrated patch and slot array antenna for terahertz quantum cascade lasers at 4.7 THz," Appl. Phys. Lett. **104**(16), 161102 (2014).

19. M. Mbonye, R. Mendis, and D. M. Mittleman, "Study of the impedance mismatch at the output end of a THz parallel-plate waveguide," Appl. Phys. Lett. **100**(11), 111120 (2012).

20. K. Wang and D. M. Mittleman, "Metal wires for terahertz wave guiding," Nature **432**(7015), 376–379 (2004).

21. K. Nielsen, H. K. Rasmussen, A. J. L. Adam, P. C. Planken, O. Bang, and P. U. Jepsen, "Bendable, low-loss Topas fibers for the terahertz frequency range," Opt. Express **17**(10), 8592–8601 (2009).

22. M. S. Vitiello, J.-H. Xu, M. Kumar, F. Beltram, A. Tredicucci, O. Mitrofanov, H. E. Beere, and D. A. Ritchie, "High efficiency coupling of Terahertz micro-ring quantum cascade lasers to the low-loss optical modes of hollow metallic waveguides," Opt. Express **19**(2), 1122–1130 (2011).

23. M. S. Vitiello, J.-H. Xu, F. Beltram, A. Tredicucci, O. Mitrofanov, J. A. Harrington, H. E. Beere, and D. A. Ritchie, "Guiding a terahertz quantum cascade laser into a flexible silver-coated waveguide," J. Appl. Phys. **110**, 063112 (2011).

24. U. Siciliani de Cumis, J.-H. Xu, C. M. Bledt, J. A. Harrington, A. Tredicucci, and M. S. Vitiello, "Flexible, Low-loss Waveguide Designs for Efficient Coupling to Quantum Cascade Lasers in the Far-infrared," J. Infrared Millimi. Thz Waves **33**(3), 319–326 (2012).

25. R. Degl'Innocenti, Y. D. Shah, D. S. Jessop, Y. Ren, O. Mitrofanov, H. E. Beere, and D. A. Ritchie, "Hollow metallic waveguides integrated with terahertz quantum cascade lasers," Opt. Express **22**(20), 24439–24449 (2014).

26. F. Castellano, H. Beere, A. D. Ritchie, and M. S. Vitiello, "Polymeric waveguide components for THz quantum cascade laser outcoupling," Proc. SPIE **8985**, 89851F (2014).

27. P. D. Cunningham, N. N. Valdes, F. A. Vallejo, L. M. Hayden, B. Polishak, X. Zhou, J. Luo, A. K.-Y. Jen, J. C. Williams, and R. J. Twieg, "Broadband terahertz characterization of the refractive index and absorption of some important polymeric and organic electrooptic materials," J. Appl. Phys. **109**(4), 043505 (2011).

28. B. S. Williams, S. Kumar, Q. Hu, and J. L. Reno, "Operation of terahertz quantum-cascade lasers at 164 K in pulsed mode and at 117 K in continuous-wave mode," Opt. Express **13**(9), 3331–3339 (2005).

29. S. Fathololoumi, E. Dupont, C. W. I. Chan, Z. R. Wasilewski, S. R. Laframboise, D. Ban, A. Mátyás, C. Jirauschek, Q. Hu, and H. C. Liu, "Terahertz quantum cascade lasers operating up to 200 K with optimized oscillator strength and improved injection tunneling," Opt. Express **20**(4), 3866–3876 (2012).